Rare Met. (2021) 40(4):848–857
https://doi.org/10.1007/s12598-020-01378-5

RARE METALS
www.editorialmanager.com/rmet

Surface-engineered gadolinium oxide nanorods and nanocuboids for bioimaging

Nitya Ramesh Chawda, Santosh Kumar Mahapatra, Indrani Banerjee*

Received: 21 January 2019 / Revised: 27 May 2019 / Accepted: 10 February 2020 / Published online: 4 April 2020

Abstract Folic acid and D-gluconic acid-capped gadolinium oxide nanorods and nanocuboids were synthesized via co-precipitation method. Comparative study of relaxivity factor on the role of capping and morphology for enhancing contrast ability for T_1 and T_2 magnetic resonance imaging (MRI) was investigated. The obtained r_2/r_1 ratio for folic acid and D-gluconic acid-capped gadolinium oxide nanorods and nanocuboids was 1.5 and 1.3, respectively. The nanocrystals were characterized and presented with properties such as good dispersity and stability required for standard contrast agent used in MRI. The characterization and the analysis of capping agent for nanocrystals suggest the preferable use of carbohydrate moieties with higher number of hydroxyl functional group reacted with urea and hydrogen peroxide for desired morphology and anisotropic growth. Thermogravimetric–differential thermal analysis (TG–DTA) illustrated the amount of capping, transition temperature from $Gd(OH)_3$ to GdOOH and crystallization temperature from GdOOH to Gd_2O_3. These nanocrystals would be significant for other biomedical applications such as drug delivery when equipped with well-functionalized drug molecules.

Keywords Contrast agent; Nanomaterials; Magnetic resonance imaging; Imaging

N. R. Chawda, I. Banerjee*
School of Nano Sciences, Central University of Gujarat, Gandhinagar 382030, India
e-mail: indrani.banerjee@cug.ac.in

S. K. Mahapatra
Department of Physical Sciences, Central University of Punjab, Bathinda 151001, India

1 Introduction

The progression of time has brought enormous advancement, understanding and development of nanosciences and nanotechnology [1]. There are several different synthesis methods already established which have found few necessary timely modification for synthesizing desired nanoparticles (NPs) [2–4]. These have contributed to the advancement in biomedical sciences toward effective diagnosis, therapy and elimination of diseases time to time [5]. In spite of such advanced developed techniques and different nanostructures, there are still certain drawbacks which need to be addressed in engineering of desired nanomaterials. Engineering of one-dimensional (1D) nanostructures (NSs) such as nanotubes, nanobelts, nanorods, nanocuboids and nanowires is highly promising biomedical tools due to their cell-specific interaction mechanism [6]. The rare earth elements have always been attractive and encouraging contenders for obtaining significant properties. The trivalent state of rare earth ions holds chemical, biophysical, electronic, optical and biomedical-sensitive characteristics due to their 4f electrons [7, 8]. The Gd^{3+} being paramagnetic in nature is widely used as the contrast agent in magnetic resonance imaging (MRI). This necessitates to synthesize more stable samples [9–11]. Generally, the synthesis route used for 1D nanosheets is hydrothermal with addition of few of the surfactants at high temperatures [12–14]. The lanthanide nanorods formed by hydrothermal technique follow oriental attachment mechanism but lack even surface and edges which would be detrimental for biomedical applications [15]. Along with anisotropic shape of nanorods, their properties and chemical reactivity are also anisotropic, due to higher positive curvature region with higher

energy [16–18]. Therefore, harmful phenomenon like dissolution or etching starts from the end surface of the rods which could have been overcome through proper surface functionalization. In contrast, the water-based wet-solution systems are comparatively cost-effective, benign, simple to handle and extremely effective for fabrication of anisotropic lanthanide nanomaterials [19, 20]. The present work emphasizes on the effects of surface capping agent by keeping other parameters constant for bioimaging application of MRI. Folic acid (FA) and D-gluconic acid (GA) were preferably used for obtaining anisotropic morphology for the FA and GA-capped Gd_2O_3 samples.

2 Experimental

2.1 Materials

Gadolinium nitrate hexahydrate ($Gd(NO_3)_3{\cdot}6H_2O$) and D-gluconic acid solution (49 wt%–53 wt% in H_2O) were purchased from Sigma-Aldrich. Folic acid was bought from HiMedia Chemicals, India. Sodium hydroxide (NaOH) and hydrogen peroxide (30% in weight to volume ratio) were procured from S.D. Fine Chem. Ltd, Mumbai, India, Urea was procured from Rankem (Delhi, India). All the chemicals were used without further purification.

2.2 Synthesis of gadolinium oxide nanorods (NRs) and nanocuboids (NCs)

The bare, folic acid (FA) and D-gluconic acid (GA)-capped gadolinium oxide (Gd_2O_3) nanorods (NRs) and nanocuboids (NCs) were synthesized using simple co-precipitation method at $\sim$ 90 °C. The synthesis involved two steps. In the first step, aqueous solutions of NaOH were added to aqueous solution of $Gd(NO_3)_3$ dropwise at the rate of 60 $\mu l{\cdot}min^{-1}$ under stirring speed of 900 $r{\cdot}min^{-1}$ at room temperature (RT). The first step used NaOH as precipitating agent for formation of $Gd(OH)_3$ which started to grow anisotropically when kept for aging. The alkaline pH has promoted the initial growth, while the second step involved the use of urea and H_2O_2 to form an adduct for controlled release of oxygen from H_2O_2. This is required for oxidation of $Gd(OH)_3$ to Gd_2O_3. The capping agent used in the same step assisted in controlling the morphology and anisotropy. The detailed study and mechanism are discussed in the next section.

2.3 Synergistic effects and mechanism of urea, H_2O_2 and capping agent

Though folic acid (FA) and glucuronic acid have been extensively used as capping agent for NSs, the obtained nanostructure was found to be agglomerated [21]. While the use of D-gluconic acid (GA) is scarce in spite of being cost-effective and benign when compared to folic acid and glucuronic acid, there are promising results with GA when used as capping agent [22–25]. Figure 1 shows the mechanism of the chemical structure of FA (Fig. 1a) and GA (Fig. 1b). The preferred functional part of capping agent through which the ligand coordination over the surface of nanoparticles happens is the carboxylate ($–COO^-$) functional group [26]. In case of folic acid, glutamate is the preferred functional part for the attachment to the surface of Gd_2O_3 via carboxylate ($–COO^-$) functional group, but the structure of GA possesses six hydroxyl functional groups and therefore has more preferred sites of interaction with urea and hydrogen peroxide which assist for ease of binding [27].

In addition to the above-mentioned mechanical and technical procedures required in growth and capping, the Brownian motion of the ions resulting from the continuous stirring of reaction mixture for on-going synthesis procedure tends the particles to colloid and assists for their coalescence to grow in elongated direction via common crystallographic orientation. The present growth of nanoparticles in such an organized manner could be anticipated by the choice of reaction time, suitable capping agent, temperature, etc., among the known reaction parameters. In particular, the combination of sugar and urea providing synergistic effect on the growth and morphology of the synthesized materials has been reported by Gawali et al. [28] for synthesis of dynamically arrested micelles. Similar synergy between D-gluconic acid and urea along with hydrogen peroxide could be useful for the anisotropic and morphological benefits which could develop smooth surfaces and sharp edges of the nanostructures [28]. The reason for such a synergy could be due to the nature of urea being simultaneous hydrophobic and hydrophilic which can easily establish bonds with hydrogen peroxide and also stabilize the nanostructure as capping agent [29]. The similar results were also observed by the use of ethanol by Gupta et al. [30], where ethanol has played a significant role for morphological and anisotropic changes assisted by the hydroxyl functional group present in the ethanol moiety. However, ethanol cannot be used as capping agent and the single hydroxyl functional groups cannot assist to the extent which the carbohydrates can perform as discussed earlier.

In addition to this multiple hydroxyl, functional groups in carbohydrate can provide enhanced biocompatibility and engineering of desired morphology and anisotropy of the nanostructures. Similarly, the uses of urea and glycerol have also been reported for the spherical nanostructures, but the use of hydrogen peroxide is equally important in the reaction medium [31, 32]. To the best of our knowledge, no

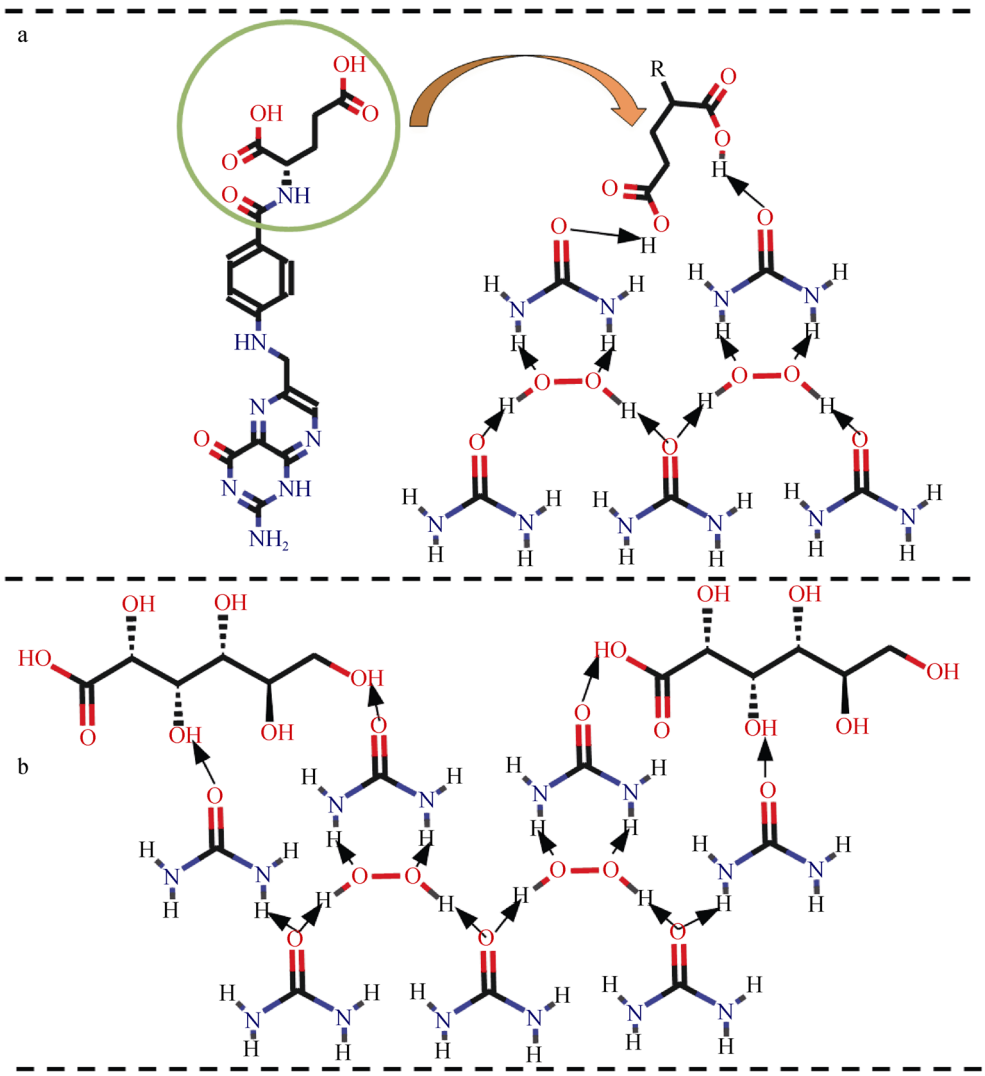

Fig. 1 Representation of glutamate structure (green-colored circle) of folic acid with its structural interaction between glutamate (folic acid), urea and H_2O_2, **a**, **b** structural interaction between D-gluconic acid, urea and H_2O_2 (this interaction is between hydrogen bonding (- - ➤) formation within urea, hydrogen peroxide, D-gluconic acid and glutamate (folic acid); along with hydrogen bonding, there are Van der Waals (vdW) forces and few π–π interaction between all compounds to produce synergistic effects)

such mechanism has been addressed thoroughly, but the role of hydroxyl functional groups of any carbohydrate or alike molecules cannot be neglected [30]. The as-synthesized samples are abbreviated as B-Gd, F-Gd and G-Gd for bare, folic acid and D-gluconic acid-capped gadolinium oxide nanorods and nanocuboids and addressed as nanoparticles (NPs) or nanocrystals in general terms wherever required.

2.4 Characterization of B-Gd, F-Gd and G-Gd

X-ray diffraction (XRD) pattern of samples was performed on PANalytical X'Pert Pro instrument of Cu Kα wavelength (λ = 0.154 nm) scanned over a 2θ range of 20°–80° with a step size of 1.25° and scan rate of 0.01 (°)·s^{-1}. Morphology of synthesized samples studied using field-emission scanning electron microscopy (FESEM, QUANTA 200 FEG, FEI, Netherlands) was used. Surface capping of samples was studied using Fourier transform infrared spectroscopy (FTIR, PerkinElmer Spectrum 65 series of FTIR spectrophotometer, USA) and thermogravimetric differential thermal analysis (TG–DTA, thermoanalyzer TG/DTA 73000, EXSTAR) using platinum crucible under inert N_2 atmosphere at 10 K·min^{-1} and temperature range from room temperature to 1000 °C. Acid digestion method was used to estimate Gd^{3+} concentration from B-Gd, F-Gd and G-Gd samples. In a typical procedure, nitric acid (HNO_3 70 vol%) was added dropwise to the samples by keeping them over open flame till a transparent and clear solution was obtained. All the

samples were later dissolved in ~ 2.5 vol% HNO_3 for further estimation of desired Gd^{3+} using a PerkinElmer inductively coupled plasma optical emission spectrometer (ICP–OES) system.

2.5 In vitro magnetic resonance imaging

T_1 relaxivity of water protons in the presence of B-Gd, F-Gd and G-Gd was measured using Siemens Magnetom Essenza 1.5 T MRI human scanner (Erlangen, Germany). The water-dispersed powdered samples in standard 1.5-ml Eppendorf tubes were used as phantoms for taking the MRI images. In vitro phantom image was collected for the B-Gd, F-Gd and G-Gd at different concentrations. The repetition time (TR) values were fitted ($1/T_1$ vs Gd concentration) to obtain a linear plot. The relaxivity value of r_1 from the slope was obtained. The parameters used for r_1 mapping by a spin echo pulse sequence to obtain image are as follows: slice thickness of 2 mm, matrix size of 676 mm × 676 mm, number of slices 5, echo time (*TE*) of 9 ms and repetition time (*TR*) values of 200, 400, 800, 1600 and 3200 ms. Saturation recovery (*S*) equation was used to obtain R_1 [33]:

$$S = S_0\left(1 - e^{-(TR \cdot R_1)}\right) + c \quad (1)$$

where S_0 is the magnetization at equilibrium, R is the rate of relaxation, and c is compensation term of the noise in measurement of data.

Relaxivity of the samples is determined by the rate of relaxation (R) as a function of concentration (C) according to the following equation [34]:

$$r_{1,2} = \frac{R_{1,2}}{C} \quad (2)$$

3 Results and discussion

3.1 Powdered XRD analysis

Figure 2 illustrates powdered XRD patterns of B-Gd, F-Gd and G-Gd samples annealed at 400 °C in air. The crystal structure and phase purity are identified by XRD patterns. All the samples consist of the mixtures of amorphous and crystalline phase. The fitted diffraction patterns of samples could be indexed to JCPDF No. 43-1014, JCPDS No. 12-0797 of cubic Gd_2O_3 and PDF-083-2037 of $Gd(OH)_3$ and Refs [35–37]. The cubic Gd_2O_3 peaks (#) corresponding to (211), (222), (400), (411), (332), (134) and (440) planes are identified. Less intense peaks of $Gd(OH)_3$ (*) corresponding to (101), (110) and (200) planes are also observed. The peak broadening is presumed to be due to the size effect and random orientation of the nanostructures

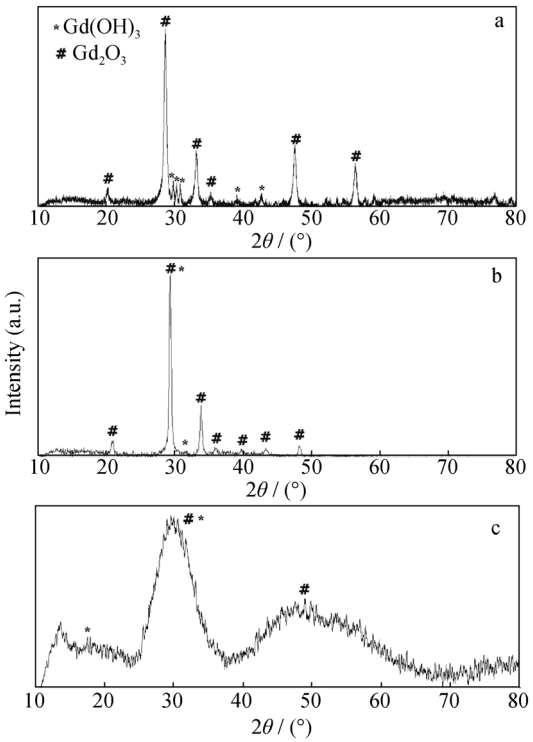

Fig. 2 XRD patterns of **a** B-Gd, **b** F-Gd and **c** G-Gd annealed at 400 °C

during measurements [37]. The surface capping has enforced changes observed in the peak position in XRD patterns, hence confirming changes in crystallographic phase formation and completeness of the reaction.

3.2 Growth mechanism and micrographs via FESEM

The nucleation and growth leading to the anisotropic morphology is predicted to be through oriental attachment mechanism. Hazarika et al. [15] have discussed about the growth of Gd_2O_3 using hydrothermal method without using capping agent. On completeness, the samples are well-defined nanorods. However, in the present synthesis process, capping agents play very important role for the morphology. FA-capped samples are nanorods, whereas GA-capped samples are nanocuboids. FESEM micrographs at different stages of synthesis were used to understand and support the morphological evaluation into anisotropic nanostructure. Figure 3 shows morphological changes occurring at different stages of the synthesis process.

The bonding between urea and hydrogen peroxide with respective capping agents GA and FA at their respective reaction conditions is found to assist the formation of desired anisotropy and morphology. The hydroxyl functional groups present in FA and GA structures interact with urea and H_2O_2 to produce synergistic effect for controlling reaction rate, chemical stability, aqueous dispersity,

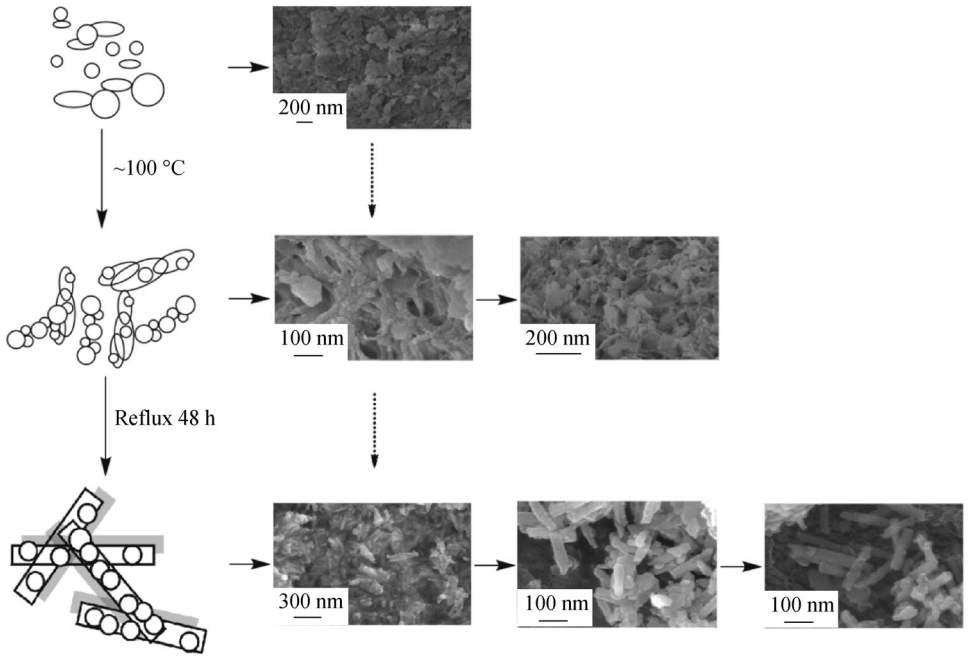

Fig. 3 Synthesis mechanism for anisotropic growth

morphology and anisotropic growth (Fig. 1) [28]. The nanostructures obtained via the present synthesis route at the final stage are ~ 200 nm in length and ~ 20 nm in diameter for F-Gd and ~ 800 nm in length and ~ 425 nm in diameter for G-Gd samples, respectively. The anisotropic growth mechanism is governed by oriented attachment followed for both F-Gd and G-Gd samples [15]. The formation mechanism of NRs and NCs follows generation of particle seeds and followed by their coalescence along a preferred direction, resulting in elongated morphology through surface effects once their common boundaries got eliminated. The responsible forces and factors driving the anisotropic growth could be preferably dipole–dipole interaction (assisted via capping agent present in reaction mixture), perfect lattice match and fusing of adjoining interface between the particles [15]. Figure 4 shows FESEM image of the final synthesized samples of B-Gd, F-Gd and G-Gd. Figure 4a shows morphology of the bare samples. The particles are mostly coagulated with partial distribution of nanostructures. Figure 4b shows FESEM image for FA-capped sample. The presence of FA as capping agent assists uniform dispersity to produce the nanorods, maintaining their anisotropy and complete growth. Figure 4c shows FESEM image for GA-capped sample. Figure 4c shows uniform growth of nanocuboids with smooth surface and sharp edges. Moreover, F-Gd NRs show surface roughness in comparison with G-Gd NCs. The role of capping agents and the functional groups on morphology of the synthesis of nanocrystals are observed. As the glutamate part of FA consists of only two hydroxyl functional groups, they do not have more preferred site of interaction with the media of synthesis, i.e., urea and hydrogen peroxide, whereas GA has six hydroxyl functional groups to control the reaction and surface simultaneously along with other properties for the growth and nucleation of the nanocrystals (Fig. 1). Therefore, F-Gd sample gets restricted to nanorods, whereas G-Gd sample possesses well-defined cuboid structure with sharp and smooth edges. Although the synthesized nanostructures are big enough for in vivo studies, the understanding of the

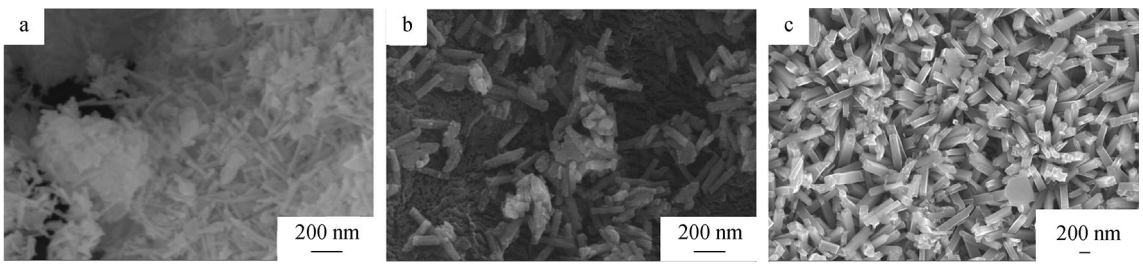

Fig. 4 FESEM images of **a** B-Gd, **b** F-Gd and **c** G-Gd

growth morphology and the shape of the nanostructures will be utilized for controlling the desired size.

3.3 TGA results

TGA was used to monitor the reaction phase transition and surface tailoring-mediated capping agent. The as-synthesized sample of B-Gd, F-Gd and G-Gd was analyzed for average weight loss to evaluate changes in phase transition and changes in the amount of capping agent for the experimental condition used for the samples. Figure 5 shows TGA plots of the samples where the transformation of gadolinium hydroxide to gadolinium oxide via distinct weight loss is observed. For B-Gd, F-Gd and G-Gd samples, the initial weight loss is attributed to the surface dehydration found at ~ 100, ~ 74 and ~ 110 °C, respectively. More distinct and multiple peaks at ~ 110, ~ 175 and ~ 221 °C are observed in G-Gd sample as compared to B-Gd and F-Gd. The peaks confirm the enhanced surface bonding via carboxylate functional group and role of extra hydroxyl functional group present in G-Gd samples as compared to B-Gd and F-Gd. In G-Gd sample (Fig. 1), the role of available six hydroxyl groups in GA promotes more surface interaction in contrast to FA in F-Gd which has fewer hydroxyl groups. Two noteworthy weight losses are observed after the removal of moisture and other loosely bound gases for rare earth oxides. As reported, rare earth oxides exist in the form of LnOOH ions [38]. The phase transition of $Gd(OH)_3$ to intermediate phase of GdOOH takes place in the form of $Gd(OH)_3 \rightarrow GdOOH + H_2O$ for which corresponding derivative thermogravimetric (DTG) peaks are at ~ 332, ~ 337 and ~ 380 °C for B-Gd, F-Gd and G-Gd samples [39–41].

The observed shift in intense DTG peaks could be addressed to the role of capping and their surface hydroxyl groups present in the capping agent who could interfere with the patterns of thermal changes. As observed in the chemical structure of both the capping agents in Fig. 1, there are few hydroxyl functional groups in FA, whereas GA possesses sufficient hydroxyl functional group. In addition to this, the bulky nature of FA has less intimacy with the nanostructure surface and does not assist strong bonding compared to GA, and in turn, it is easy to cleave its attached bonds, resulting in lowering of corresponding transition temperatures of the DTG peaks [41]. The number of hydroxyl functional groups in GA compared to FA is more than double, and therefore, these groups distributed in all sides of its structure, which provides enhanced stability

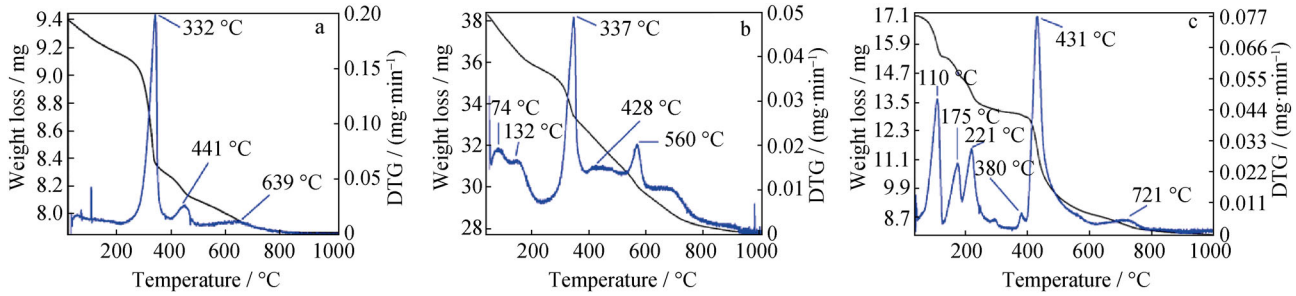

Fig. 5 TGA analysis of **a** B-Gd, **b** F-Gd and **c** G-Gd

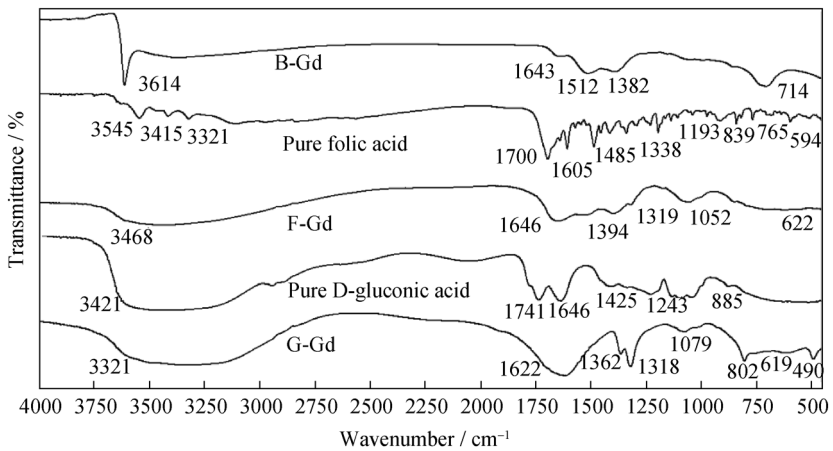

Fig. 6 FTIR spectra of B-Gd, pure folic acid, F-Gd, pure D-gluconic acid and G-Gd

Table 1 Assignment of vibrational stretching frequency peaks

Samples	Peak/cm^{-1}	Assignment
B-Gd	3614	$(OH)_S$
	1512	$(NH)_B/(C=C)_S$
	1382	$(COOH)_{SS}$
	1060	$(CO)_S$
	814	$(GdO)_S$
	714	Gd–O–H
Folic acid	3545	$(OH)_S$
	3415	$(OH)_S$
	3321	$(OH)_S$
	1700	$(COOH)_{AS}/(C=O)_S$
	1605	$(COOH)_{AS}/(C=O)_S$
	1485	$(COOH)_{SS}$
	1338	$(NH)_B/(C=C)_S$
	1193	$(CO)_S$
	839, 765, 594	$(> CH_2)_S$
F-Gd	3468	$(OH)_S$
	1646	$(C=O)_S$
	1319	$(C–H)_B$
	1394	$(C–OH)_S/(CH_2)_T$
	1052	$(CO)_S$
	622	$(GdO)_S$
	714	Gd–O–H
D-gluconic acid	3421	$(OH)_S$
	1741	$(COOH)_{AS}$
	1646	$(COOH)_{AS}/(C=O)_S$
	1440	$(COOH)_{SS}$
	1243	$(C–OH)_S$
	885	$(> CH_2)_S$
G-Gd	3321	$(OH)_S$
	1622	$(C=O)_S$
	1318	$(C–H)_B$
	1362	$(C–OH)_S/(CH_2)_T$
	1079	$(CO)_S$
	802,619,490	$(GdO)_S$
	714	Gd–O–H

S stretch, SS symmetric stretch, AS asymmetric stretch, B bend, T twisting

along with controlled morphology. The second step of dehydration in the form of $2GdOOH \rightarrow Gd_2O_3 + H_2O$ is observed at ~ 441, ~ 428 and ~ 431 °C for B-Gd, F-Gd and G-Gd samples, respectively [42]. The complete conversion of $Gd(OH)_3$ to Gd_2O_3 could be observed beyond ~ 560 °C for all the samples [43]. The corresponding DTG peaks are obtained at ~ 639, ~ 560 and ~ 721 °C for B-Gd, F-Gd and G-Gd samples, respectively. The lower transition temperature for F-Gd sample is due to weaker binding and melting point (m.p.)

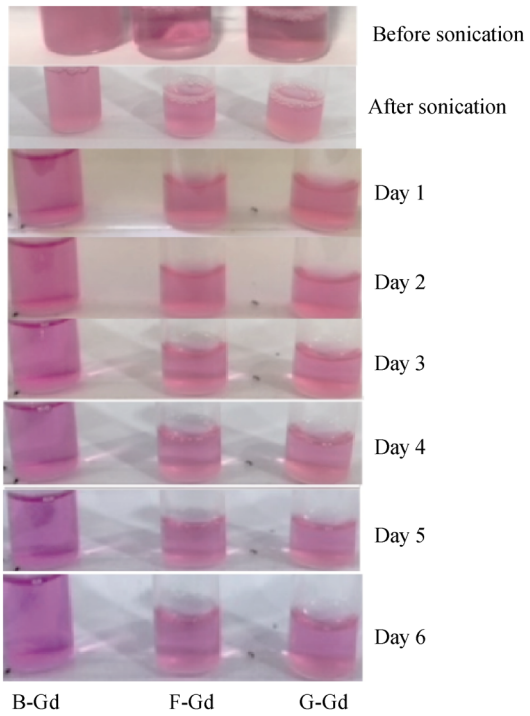

Fig. 7 Stability of B-Gd, F-Gd and G-Gd samples for 6 d in biological medium

of FA (m.p. 250 °C) in comparison with GA (m.p. 131 °C) as discussed earlier. The capping amount was calculated by the weight loss and remaining weight of sample after moisture removal. A loss of 0.05 mg·mg^{-1} till 260 °C is accounted for the melting of surface capping for FA whose melting point is 250 °C. Similarly, a loss of 0.066 mg·mg^{-1} till 221 °C can be observed from DTG apparent peak beyond 131 °C which is the melting point of GA.

3.4 Fourier transform infrared spectroscopy (FTIR) analysis

Figure 6 illustrates comparative FTIR spectra for B-Gd, F-Gd and G-Gd samples. The observed vibrational frequencies are tabulated in Table 1.

The stretching frequency spectra of B-Gd, folic acid, F-Gd, D-gluconic acid (GA) and G-Gd are compared for the surface capping studies by the used ligands for enhancing surface morphology, biocompatibility and anisotropic growth. Stretching frequencies at ~ 3614, 3545, 3415, 3321, 3468, 3421 and 3321 cm^{-1} are attributed to O–H stretching vibration ($\upsilon(OH_{water})$) due to absorbed water and mixed hydroxide. Stretching frequencies corresponding to free –COOH bonds are observed around 1700–1745 cm^{-1} (C=O). Similar pattern of bonding through –COOH is also found in reported literature over metal oxide surfaces [11, 28, 44]. The mode of

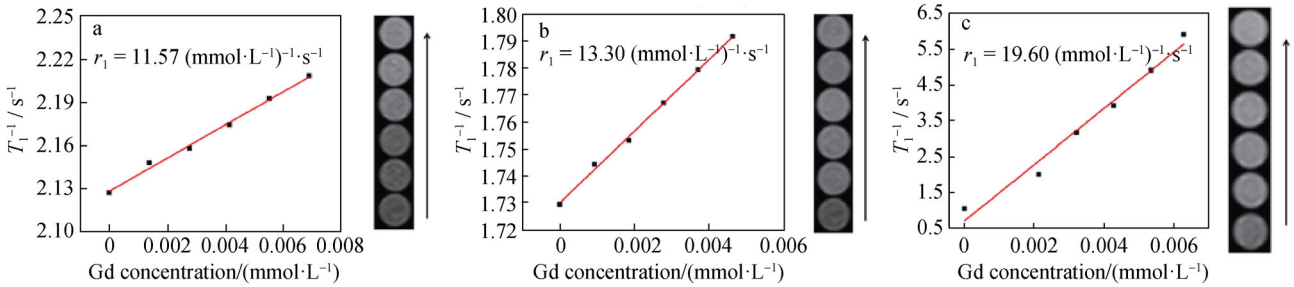

Fig. 8 Plots of $1/T_1$ as a function of Gd concentration of **a** B-Gd, **b** F-Gd and **c** G-Gd with their respective in vitro phantom images at different Gd concentrations

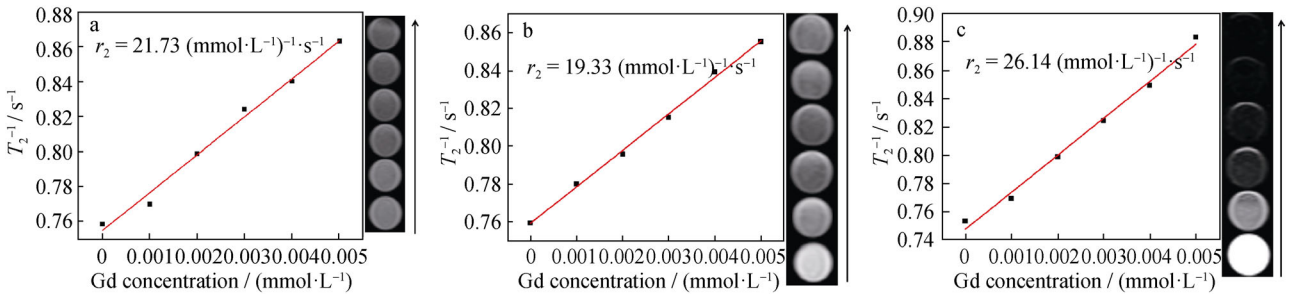

Fig. 9 Plots of $1/T_2$ as a function of Gd concentration of B-Gd **a** F-Gd **b** and G-Gd **c** with their respective in vitro phantom images at different Gd concentrations

Table 2 r_1 and r_2 values of samples

Samples	r_1/[(mmol·L^{-1})$^{-1}$·s^{-1}]	r_2/[(mmol·L^{-1})$^{-1}$·s^{-1}]	r_2/r_1
B-Gd	11.57	21.73	1.9
F-Gd	13.30	19.33	1.5
G-Gd	19.60	26.14	1.3

attachment is confined to single oxygen atom as without single oxygen atom capping, the symmetric CO_2− stretching should have been detected in the range of 1400–1450 cm^{-1} [31, 34]. Stretching frequencies at ∼ 1700, 1741 and 1425 cm^{-1} in pure FA and GA spectra are observed, indicating –COOH and symmetric CO_2^- stretching in free forms.

The peaks get red-shifted by ∼ 54 and ∼ 119 cm^{-1} for both the capped samples, respectively, appearing around ∼ 1646 and ∼ 1622 cm^{-1} again, confirming the capping through single oxygen atom of carboxyl mode of attachment. Pure FA samples show amide-I peak at ∼ 1605 cm^{-1} corresponding to N–H stretching and vibration, amide-III peak at ∼ 1338 cm^{-1} for C-O stretching vibration at ∼ 1193 cm^{-1} and C–C stretching vibration at ∼ 800–600 cm^{-1} [45]. The peak shifting in this domain can be regarded as conclusive support for successful capping of FA over Gd_2O_3 surface. Spectra for G-Gd sample show C-H bending of the ligand at ∼ 1362 and ∼ 1318 cm^{-1}, stretching vibration of C–O at ∼ 1079 cm^{-1}. The peaks at ∼ 802, ∼ 619 and ∼ 490 cm^{-1} correspond to typical Gd-O bonding in G-Gd sample [43]. The board IR peak around ∼ 714 cm^{-1} observed in B-Gd, F-Gd and G-Gd corresponds to O–H bending of Gd-O–H [46].

3.5 Stability in biological fluids

Figure 7 shows the stability of the samples for 6 days. The stability of B-Gd, F-Gd and G-Gd samples was carried out in standard Roswell Park Memorial Institute (RPMI) medium with 10% fetal bovine *serum* (FBS). The F-Gd and G-Gd samples are found to be stable compared to B-Gd.

3.6 In vitro MRI images

Gadolinium-based material is widely used as efficient probe for MRI. However, surface leaching of Gd^{3+}, surface roughness, dispersibility, etc., affect its functions and are proved to be detrimental. The leaching studies using ICP-OES show no significant leaching of Gd^{3+}. Comparative study of the effect of surface functionalization using FA and GA is to be studied for MRI application. Figures 8 and

9 show the linear plot map of inverse longitudinal relaxation time ($1/T_1$ (s^{-1})) and transverse relaxation time ($1/T_2$ (s^{-1})) versus Gd concentration (mmol·L^{-1}) under the applied magnetic field of 1.5 T for all samples. B-Gd, F-Gd and G-Gd samples were tested and compared for proton relaxivity (r_1 and r_2). The r_1 and r_2 values determined for B-Gd, F-Gd and G-Gd samples are 11.57, 13.30, 19.60 and 21.73, 19.33 and 26.14 $(mmol{\cdot}L^{-1})^{-1}{\cdot}s^{-1}$, respectively, and tabulated in Table 2. The report by Fang et al. [47] reveals that surface capping agent with hydrophilic ligands is more efficient than hydrophobic ligands. Therefore, on virtue of easy and natural access to surrounding water molecules, they used polyvinylpyrrolidone (PVP) as capping agent by replacing oleic acid. Generally, T_1-weighted agents exhibit high r_1 values and low r_2/r_1 ratios, whereas T_2-weighted agents express considerably lower r_1 than r_2, resulting in high r_2/r_1 ratios for negative MRI contrast enhancement [48]. In the present study, G-Gd shows minimum value of r_2/r_1 ratio of 1.3 as compared to F-Gd and B-Gd which have the values of 1.5 and 1.9, respectively. G-Gd sample with less bulky functional group compared to F-Gd supports easy access to the nearby water molecules for relaxation, and therefore, G-Gd sample shows 70% enhancement of r_1 value, whereas F-Gd shows 15% increase with respect to B-Gd sample.

The calculated r_1 values for samples are four times larger than the commercially used clinical contrast agent Magnevist® (4 $(mmol{\cdot}L^{-1})^{-1}{\cdot}s^{-1}$) at the same magnetic field strength of 1.5 T [48, 49]. The contrast of the image represented by T_1 images always starts from dark to gray with the increase in concentration of gadolinium compounds. Figures 8 and 9 show the comparative T_1 and T_2 images of the B-Gd, F-Gd and G-Gd samples, which starts as the darker image at 0 $mg{\cdot}ml^{-1}$ concentration and increases in its gray-colored intensity.

The contrast of the T_1-weighted phantoms of the same concentration seems to be much enhanced for G-Gd samples as compared to F-Gd and B-Gd samples. As discussed earlier, the as-synthesized samples possess different morphologies with difference in surface chemistry. Large fraction of Gd atoms present on the surface leads to an increase in average magnetic moment per atom. Therefore, the T_1 relaxation (longitudinal relaxation) time of water protons in its near vicinity gets lowered while increasing the contrast.

4 Conclusion

The effect of surface functionalization using FA and GA along with possible mechanism for anisotropic growth of lanthanide-based oxide was discussed. FA-capped samples formed nanorods, whereas GA-capped samples were nanocuboids. The transition and crystallizing temperature for the conversion of the lanthanides from the hexagonal phase to cubic phase was found to be affected by surface engineering. The samples were tested as MRI contrast agent, where G-Gd sample showed 70% enhancement of r_1 value, whereas F-Gd showed 15% increase with respect to B-Gd sample. The need of morphology and shape of nanomaterials for biomedical applications were also highlighted.

Acknowledgements The authors wish to acknowledge Central University of Gujarat, Gandhinagar, and Central University of Punjab, Bathinda, for providing infrastructure and instrumentation facility for the present work.

References

[1] Ezema IC, Ogbobe PO, Omah AD. Initiatives and strategies for development of nanotechnology in nations: a lesson for Africa and other least developed countries. Nanoscale Res Lett. 2014; 9(1):133.
[2] Ding YJ, Han PD, Wang LX, Zhang QT. Preparation, morphology and luminescence properties of Gd_2O_2S: Tb with different Gd_2O_3 raw materials. Rare Met. 2019;38(3):221.
[3] Heinz H, Pramanik C, Heinz O, Ding Y, Mishra RK, Marchon D, Flatt RJ, Estrela-Lopis I, Llop J, Moya S, Ziolo RF. Nanoparticle decoration with surfactants: molecular interactions, assembly, and applications. Surf Sci Rep. 2017;72(1):1.
[4] Luo JM, Xu JL, Zhong ZC. Microstructure and properties of Y_2O_3-doped steel-cemented WC prepared by microwave sintering. Rare Met. 2013;32(5):496.
[5] Laal M. Innovation and medicine. Proc Technol. 2012;1(3):469.
[6] Liu TM, Conde J, Lipiński T, Bednarkiewicz A, Huang C-C. Revisiting the classification of NIR-absorbing/emitting nanomaterials for in vivo bioapplications. NPG Asia Mater. 2016; 8(8):295.
[7] Mahata MK, Bae H, Lee KT. Upconversion luminescence sensitized pH-nanoprobes. Molecules. 2017;22(12):2064.
[8] Chen G, Qiu H, Prasad PN, Chen X. Upconversion nanoparticles: design, nanochemistry, and applications in theranostics. Chem Rev. 2014;114(10):5161.
[9] Ranga A, Agarwal Y, Garg KJ. Gadolinium based contrast agents in current practice: risks of accumulation and toxicity in patients with normal renal function. Indian J Radiol Imaging. 2017;27(2):141.
[10] Rogosnitzky M, Branch S. Gadolinium-based contrast agent toxicity: a review of known and proposed mechanisms. Biometals. 2016;29(3):365.
[11] Ibrahim MA, Dublin AB. Magnetic resonance imaging (MRI), gadolinium. Treasure Island: StatPearls; 2019. 1.
[12] Berven CA, Dobrokhotov VV. Towards practicable sensors using one-dimensional nanostructures. Int J Nanotechnol. 2008; 5(4/5):402.
[13] Shanmugasundaram A, Ramireddy B, Basak P, Manorama SV, Srinath S. Hierarchical $In(OH)_3$ as a precursor to mesoporous In_2O_3 nanocubes: a facile synthesis route, mechanism of self-assembly, and enhanced sensing response toward hydrogen. J Phys Chem C. 2014;118(13):6909.
[14] Liu JW, Xu J, Hu W, Yang JL, Yu SH. Systematic synthesis of tellurium nanostructures and their optical properties: from nanoparticles to nanorods, nanowires, and nanotubes. ChemNanoMat. 2016;2(3):167.

[15] Hazarika S, Mohanta D. Oriented attachment (OA) mediated characteristic growth of Gd_2O_3 nanorods from nanoparticle seeds. J Rare Earths. 2016;34(2):158.
[16] Reguera J, Langer J, Jiménez de Aberasturi D, Liz-Marzán LM. Anisotropic metal nanoparticles for surface enhanced Raman scattering. Chem Soc Rev. 2017;46(13):3866.
[17] Wu B, Liu D, Mubeen S, Chuong TT, Moskovits M, Stucky GD. Anisotropic growth of TiO_2 onto gold nanorods for plasmon-enhanced hydrogen production from water reduction. J Am Chem Soc. 2016;138(4):1114.
[18] Castelli A, Striolo A, Roig A, Murphy C, Reguera J, Liz-Marzán L, Mueller A, Critchley K, Zhou Y, Brust M, Thill A, Scarabelli L, Tadiello L, Konig TAF, Reiser B, Lopez-Quintela MA, Buzza M, Deak A, Kuttner C, Solveyra EG, Pasquato L, Portehault D, Mattoussi H, Kotov NA, Kumacheva E, Heatley K, Bergueiro J, Gonzalez G, Tong W, Tahir MN, Abecassis B, Rojas-Carrillo O, Xia Y, Mayer M, Peddis D. Anisotropic nanoparticles: general discussion. Faraday Discuss. 2016;191:229.
[19] Gawande MB, Goswami A, Felpin FX, Asefa T, Huang X, Silva R, Zou X, Zboril R, Varma RS. Cu and Cu-based nanoparticles: synthesis and applications in catalysis. Chem Rev. 2016;116(6):3722.
[20] Iravani S, Korbekandi H, Mirmohammadi SV, Zolfaghari B. Synthesis of silver nanoparticles: chemical, physical and biological methods. Res Pharm Sci. 2014;9(6):385.
[21] Sánchez Lafarga AK, Pacheco Moisés FP, Gurinov A, Ortiz GG, Carbajal Arízaga GG. Dual responsive dysprosium-doped hydroxyapatite particles and toxicity reduction after functionalization with folic and glucuronic acids. Mater Sci Eng C. 2015;2015(48):541.
[22] Chávez-García D, Juárez-Moreno K, Campos CH, Alderete JB, Hirata GA. Upconversion rare earth nanoparticles functionalized with folic acid for bioimaging of MCF-7 breast cancer cells. J Mater Res. 2018;33(02):191.
[23] Sun X, Zheng C, Zhang F, Yang Y, Wu G, Yu A, Guan N. Size-controlled synthesis of magnetite (Fe_3O_4) nanoparticles coated with glucose and gluconic acid from a single Fe(III) precursor by a sucrose bifunctional hydrothermal method. J Phys Chem C. 2009;113(36):16002.
[24] Osorio-Román IO, Ortega-Vásquez V, Vargas CV, Aroca RF. Surface-enhanced spectra on D-gluconic acid coated silver nanoparticles. Appl Spectrosc. 2011;6598:838.
[25] Wei X, Wei Z, Zhang L, Liu Y, He D. Science Highly water-soluble nanocrystal powders of magnetite and maghemite coated with gluconic acid: preparation, structure characterization, and surface coordination. J Colloid Interface Sci. 2011;354(1):76.
[26] Ye YX, Wei LH, Sheng WC, Chen M, Hua YQ. Luminescent properties of a new Nd^{3+}-doped complex with two different carboxylic acids and pyridine derivative. Rare Met. 2013;32(5):490.
[27] Yu S, Chow GM. Carboxyl group (–CO_2H) functionalized ferrimagnetic iron oxide nanoparticles for potential bio-applications. J Mater Chem. 2004;14(18):2781.
[28] Gawali SL, Zhang M, Kumar S, Aswal VK, Danino D, Hassan PA. Dynamically arrested micelles in a supercooled sugar urea melt. Commun Chem. 2018;1(1):33.
[29] Zangi R, Zhou R, Berne BJ. Urea's action on hydrophobic interactions. J Am Chem Soc. 2009;131(4):1535.
[30] Gupta BK, Singh S, Kumar P, Lee Y, Kedawat G, Narayanan TN, Vithayathil SA, Ge L, Zhan X, Gupta S, Marti AA, Vajtai R, Ajayan PM, Kaipparettu BA. Bifunctional luminomagnetic rare-earth nanorods for high-contrast bioimaging nanoprobes. Sci Rep. 2016;6(1):32401.
[31] Zhou L, Gu Z, Liu X, Yin W, Tian G, Yan L, Jin S, Ren W, Xing G, Li W, Chang X, Hu Z, Zhao Y. Size-tunable synthesis of lanthanide-doped Gd_2O_3 nanoparticles and their applications for optical and magnetic resonance imaging. J Mater Chem. 2012;22(3):966.
[32] Zhang Q, Li N, Goebl J, Lu Z, Yin Y. A systematic study of the synthesis of silver nanoplates: is citrate a "magic" reagent? J Am Chem Soc. 2011;133(46):18931.
[33] Carneiro AAO, Vilela GR, De Araujo DB, Baffa O. MRI relaxometry: methods and applications. Braz J Phys. 2006;36(1):9–15.
[34] Koenig SH, Kellar KE. Theory of $1/T_1$ and $1/T_2$ NMRD profiles of solutions of magnetic nanoparticles. Magn Reson Med. 1995;34(2):227.
[35] Debasu ML, Ananias D, Macedo AG, Rocha J, Carlos LD. Emission-decay curves, energy-transfer and effective-refractive index in Gd_2O_3:Eu^{3+} nanorods. J Phys Chem C. 2011;115(31):15297.
[36] Tamrakar RK, Bisen DP, Robinson CS, Sahu IP, Brahme N. Ytterbium doped gadolinium oxide (Gd_2O_3:Yb^{3+}) phosphor: topology, morphology, and luminescence behaviour. Indian J Mater Sci. 2014;2014:1.
[37] Singh G, McDonagh BH, Hak S, Peddis D, Bandopadhyay S, Sandvig I, Sandvig A, Glomm WR. Synthesis of gadolinium oxide nanodisks and gadolinium doped iron oxide nanoparticles for MR contrast agents. J Mater Chem B. 2017;5(3):418.
[38] Chang C, Zhang Q, Mao D. The hydrothermal preparation, crystal structure and photoluminescent properties of GdOOH nanorods. Nanotechnology. 2006;17(8):1981.
[39] Chaudhary S, Kumar S, Umar A, Singh J, Rawat M, Mehta SK. Europium-doped gadolinium oxide nanoparticles: a potential photoluminescencent probe for highly selective and sensitive detection of Fe^{3+} and Cr^{3+} ions. Sensors Actuators B Chem. 2017;243:579.
[40] Yang J, Li C, Cheng Z, Zhang X, Quan Z, Zhang C, Lin J. Size-tailored synthesis and luminescent properties of one-dimensional Gd_2O_3:Eu^{3+} nanorods and microrods. J Phys Chem C. 2007;111(49):18148.
[41] Zhang G, Gao J, Qian J, Zhang L, Zheng K, Zhong K, Cai D, Zhang X, Wu Z. Hydroxylated mesoporous nanosilica coated by polyethylenimine coupled with gadolinium and folic acid: a tumor-targeted T_1 magnetic resonance contrast agent and drug delivery system. ACS Appl Mater Interfaces. 2015;7(26):14192.
[42] Huang S, Xu HL, Wang L, Zhong SL. Microwave-hydrothermal synthesis, characterization and upconversion luminescence of rice-like $Gd(OH)_3$ nanorods. Rare Met. 2016. https://doi.org/10.1007/s12598-016-0816-2.
[43] Kim CR, Baeck JS, Chang Y, Bae JE, Chae KS, Lee GH. Ligand-size dependent water proton relaxivities in ultrasmall gadolinium oxide nanoparticles and in vivo T_1 MR images in a 15 T MR field. Phys Chem Chem Phys. 2014;16(37):19866.
[44] Ahmad MW, Xu W, Kim SJ, Baeck JS, Chang Y, Bae JE, Chae KS, Park JA, Kim TJ, Lee GH. Potential dual imaging nanoparticle:Gd_2O_3 nanoparticle. Sci Rep. 2015;5(1):8549.
[45] Yousefi T, Torab-Mostaedi M, Ghasemi M, Ghadirifar A. Synthesis of Gd_2O_3 nanoparticles: using bulk Gd_2O_3 powders as precursor. Rare Met. 2015;34(8):540.
[46] Kang J, Min B, Sohn Y. Synthesis and characterization of $Gd(OH)_3$ and Gd_2O_3 nanorods. Ceram Int. 2015;41(1):1243.
[47] Fang J, Chandrasekharan P, Liu XL, Yang Y, Lv YB, Yang CT, Ding J. Biomaterials manipulating the surface coating of ultra-small Gd_2O_3 nanoparticles for improved T_1-weighted MR imaging. Biomaterials. 2014;35(5):1636.
[48] Huang CL, Huang CC, Mai FD, Yen CL, Tzing SH, Hsieh HT, Ling YC, Chang JY. Application of paramagnetic graphene quantum dots as a platform for simultaneous dual-modality bioimaging and tumor-targeted drug delivery. J Mater Chem B. 2015;3(4):651.
[49] Lauffer RB. Paramagnetic metal complexes as water proton relaxation agents for NMR imaging: theory and design. Chem Rev. 1987;87(5):901.